

MIT Open Access Articles

Interface pinning of immiscible gravity-exchange flows in porous media

The MIT Faculty has made this article openly available. **Please share** how this access benefits you. Your story matters.

Citation: Zhao, Benzhong et al. "Interface Pinning of Immiscible Gravity-exchange Flows in Porous Media." *Physical Review E* 87.2 (2013). ©2013 American Physical Society

As Published: <http://dx.doi.org/10.1103/PhysRevE.87.023015>

Publisher: American Physical Society

Persistent URL: <http://hdl.handle.net/1721.1/77935>

Version: Final published version: final published article, as it appeared in a journal, conference proceedings, or other formally published context

Terms of Use: Article is made available in accordance with the publisher's policy and may be subject to US copyright law. Please refer to the publisher's site for terms of use.



Interface pinning of immiscible gravity-exchange flows in porous media

Benzhong Zhao,¹ Christopher W. MacMinn,^{1,2} Michael L. Szulcowski,¹ Jerome A. Neufeld,³
Herbert E. Huppert,^{4,5} and Ruben Juanes^{1,*}

¹*Massachusetts Institute of Technology, 77 Massachusetts Ave, Building 48, Cambridge, Massachusetts, USA*

²*Department of Geology & Geophysics, Yale University, New Haven, Connecticut, USA*

³*BP Institute and Departments of Earth Sciences and Applied Mathematics and Theoretical Physics,
University of Cambridge, Madingley Road, Cambridge CB3 0EZ, UK*

⁴*Institute of Theoretical Geophysics, Department of Applied Mathematics and Theoretical Physics,
University of Cambridge, Wilberforce Road, Cambridge CB3 0WA, UK*

⁵*School of Mathematics, University of New South Wales, Kensington, Australia*

(Received 18 December 2011; revised manuscript received 14 January 2013; published 19 February 2013)

We study the gravity-exchange flow of two immiscible fluids in a porous medium and show that, in contrast with the miscible case, a portion of the initial interface remains pinned at all times. We elucidate, by means of micromodel experiments, the pore-level mechanism responsible for capillary pinning at the macroscale. We propose a sharp-interface gravity-current model that incorporates capillarity and quantitatively explains the experimental observations, including the $x \sim t^{1/2}$ spreading behavior at intermediate times and the fact that capillarity stops a finite-release current. Our theory and experiments suggest that capillary pinning is potentially an important, yet unexplored, trapping mechanism during CO₂ sequestration in deep saline aquifers.

DOI: [10.1103/PhysRevE.87.023015](https://doi.org/10.1103/PhysRevE.87.023015)

PACS number(s): 47.56.+r, 47.55.Hd, 47.55.N–

I. INTRODUCTION

Gravity-exchange flows, in which density differences induce fluid segregation and migration, occur in processes as diverse as debris flows [1], seawater intrusion into groundwater [2], and coating of substrates by thin films [3]. More recently gravity-current flows have emerged as fundamental descriptors of the fluid mechanics of carbon dioxide (CO₂) sequestration in saline aquifers [e.g., Refs. [4–10]]. While the study of gravity-exchange flows in porous media has a long history [11], they have been investigated experimentally only in the context of completely miscible fluids. Here we investigate the gravity-exchange flow of two *immiscible* fluids in a porous medium using table-top experiments in a quasi-2D transparent cell packed with glass beads.

In the classical *miscible* lock-exchange flow, two miscible fluids of different densities are initially separated by a vertical “interface.” This fluid interface evolves by tilting smoothly around a stationary point at a height h_s [Fig. 1(a)]. The classical model for this problem assumes that diffusion is slow so the fluids may be assumed to be completely segregated, and that the pressure distribution within both fluids is hydrostatic [11, 12]. A similarity solution of the classical model predicts that the tip position of the fluid interface (x) propagates with respect to time (t) as $x \sim t^{1/2}$ [11, 12], and this prediction is in excellent agreement with experiments [Fig. 1(a)].

In an *immiscible* lock-exchange flow, capillary forces strongly affect the flow behavior: We observe that a portion of the initial interface remains pinned and does not experience any macroscopic motion. Above this pinned portion of the interface the lighter fluid spreads laterally to the right, and below it the heavier fluid spreads to the left [Fig. 1(b)]. Here we show that capillary pinning is a distinct porous-medium phenomenon that requires the presence of microstructure, we explain its

pore-level origin, and we develop a sharp-interface model that is able to predict the macroscopic interface evolution of immiscible lock-exchange flow.

II. LOCK-EXCHANGE EXPERIMENTS

We conducted lock-exchange experiments in rectangular, quasi-2D flow cells packed with glass beads. We constructed four flow cells with different heights (2.5 cm, 5.2 cm, 10.3 cm, 20 cm) and the same length (~ 55 cm) and thickness (0.9 cm). Each flow cell consists of three pieces of laser-cut acrylic: solid front and rear panels and a middle spacer that frames the working area. The spacer is clamped between the front and rear panels via bolts. Once assembled, we orient the cell “vertically” [Fig. 2(a)] and fill it with glass beads via a port on the spacer. We shake the cell during filling to generate a tight, consistent bead pack. The porosity of the packed flow cell ranges from 0.38 to 0.42. Once the cell is full, we plug this port. We use non-monodisperse glass beads with nominal bead sizes ranging from 0.36 mm to 2.1 mm (Fig. 3). The permeability of the packed flow cell for 1mm beads is $0.88 \times 10^{-5} \text{ cm}^2$.

In the miscible lock-exchange experiments, we used water with blue food dye as the buoyant fluid and a mixture of glycerol and water (77.5% glycerol by mass, $\rho = 1.2 \text{ g/cm}^3$, $\mu = 0.47 \text{ g/cm-s}$) as the ambient fluid.

In the immiscible lock-exchange experiments, we used air as the buoyant fluid. We used one of silicone oil ($\rho = 0.96 \text{ g/cm}^3$, $\mu = 0.48 \text{ g/cm-s}$, $\gamma = 20 \text{ dyn/cm}$), propylene glycol ($\rho = 1.04 \text{ g/cm}^3$, $\mu = 0.46 \text{ g/cm-s}$, $\gamma = 41 \text{ dyn/cm}$), or the glycerol-water mixture (as above, $\gamma = 63 \text{ dyn/cm}$) as the ambient fluid.

We measured the advancing and receding contact angles of each of the fluid pairs used in our experiments (air and silicon oil; air and propylene glycol; and air and a glycerol-water mixture) on both glass and acrylic substrates. The measurements were made using the sessile drop method, on a ramé-hart Model 590 Advanced Automated Goniometer.

*juan@mit.edu

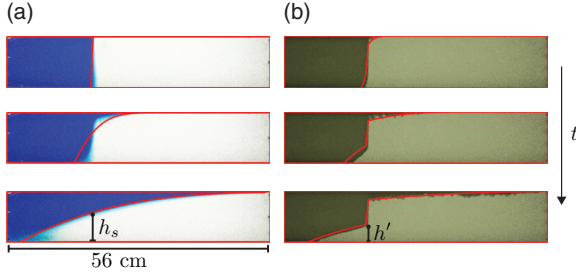


FIG. 1. (Color online) Lock-exchange flow in a porous medium with (a) miscible and (b) immiscible fluids. (a) The miscible fluids are water (blue) spreading over a denser, more viscous mixture of glycerol and water. A smooth macroscopic interface tilts around a stationary point with fixed height h_s . (b) The immiscible fluids are air (dark) spreading over the same glycerol-water mixture. Part of the initial interface remains pinned, which leads to sharp kinks or “hinges” in the macroscopic interface. We denote the height of the lower hinge by h' . Both experiments were conducted in a transparent cell packed with 1 mm glass beads. The red curves correspond to the predictions of sharp-interface models.

Figure 4 shows snapshots from the contact angle goniometer for measurements on a glass substrate. The advancing and receding contact angles of silicon oil on acrylic are both zero.

To add the fluids to the cell, we orient the cell vertically. We add the ambient fluid via a port near the bottom in the vertical orientation [Fig. 2(a)]. We inject the ambient fluid with a syringe pump in order to measure the volume injected. Once the ambient fluid is filled to the desired level, we inject the buoyant fluid via a port near the top in the vertical orientation. We then close all ports. In the immiscible lock exchange experiments, the buoyant fluid does not need to be injected because it is air.

To initiate an experiment, we quickly rotate the cell by 90° so that it lies horizontally on the table, between an LED backlight and a digital camera [Fig. 2(b)]. We record the experiment as a sequence of still images. We disassemble the cell, discard the beads, and wash the acrylic plates after each experiment.

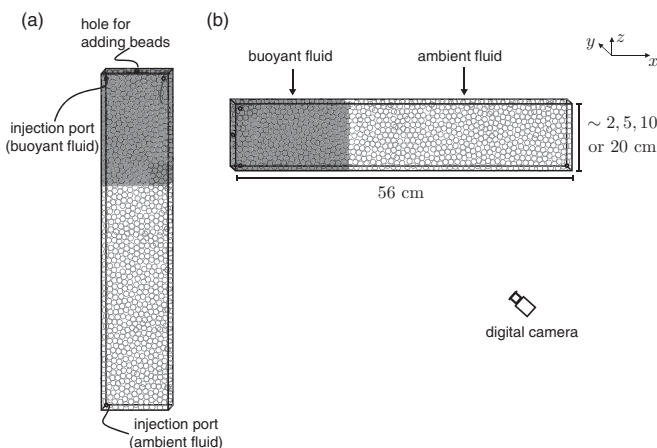


FIG. 2. Experimental setup of the lock-exchange experiments in quasi-two-dimensional flow cells packed with glass beads.

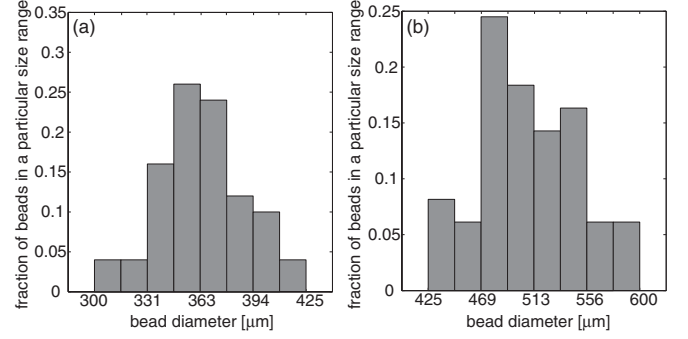


FIG. 3. Bead size distribution for two of the nominal bead sizes used in our experiments: (a) bead size 300 to 425 μm , (b) bead size 425 to 600 μm . We take the arithmetic mean of the endpoints of each range as the characteristic grain size d .

III. INTERFACE PINNING: STATICS

A. Scaling of the hinge height

We characterize capillary pinning by the height where the imbibition front meets the vertically pinned interface, which we call the hinge height, h' [Fig. 1(b)]. To determine what controls h' we perform a dimensional analysis (e.g., Ref. [13]). The variables involved in the immiscible lock-exchange flow are height of the flow cell H ; density difference between the dense and buoyant fluids, $\Delta\rho = \rho_2 - \rho_1$; corresponding fluid viscosities, μ_2 and μ_1 ; interfacial tension γ between the fluids; receding and advancing contact angles, θ_r and θ_a , respectively [14,15]; bead size d ; gravitational constant g ; and time t . In the limit of $d \ll H$ and negligible kinetic energy, dimensional analysis indicates a relation of the form $h'/H = F(\text{Bo}, \mathcal{M}, \theta_r, \theta_a)$, where $\text{Bo} = \Delta\rho g H / (\gamma/d)$ is the Bond number, which measures the relative importance of gravity to capillary forces, and $\mathcal{M} = \mu_2/\mu_1$ is the viscosity ratio between the fluids. To vary the Bond number, we vary the height of the cell, the size of the glass beads, and the interfacial tension (by changing the fluid pair). We use air (fluid 1) and a viscous liquid (fluid 2). Depending on the choice of the liquid (silicone oil, propylene glycol, or a glycerol-water mixture),

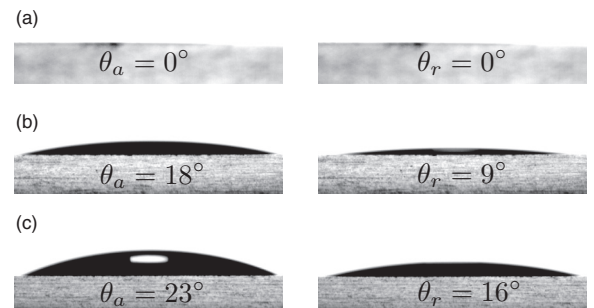


FIG. 4. Measurements of the advancing contact angle (left) and receding contact angle (right) on a glass surface for the different fluid pairs used in the experiments: (a) silicone oil, (b) propylene glycol, (c) glycerol-water mixture. The glycerol-water mixture and propylene glycol are both partially wetting to glass with respect to air, and exhibit contact angle hysteresis. Silicone oil is perfectly wetting to glass with respect to air, having advancing and receding contact angles of 0° .

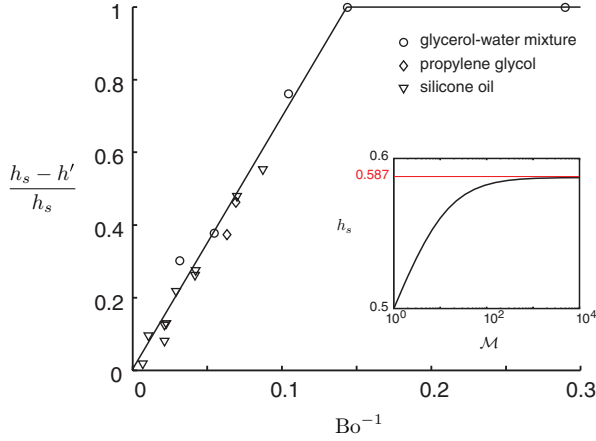


FIG. 5. (Color online) Scaling of the pinned interface height in an immiscible lock-exchange flow. We measure the deviation of the immiscible lock exchange from the miscible lock exchange via the normalized difference between the lower hinge height h' and the height of the miscible tilting point, h_s (inset), at the same value of \mathcal{M} . This quantity scales linearly with the strength of capillarity relative to gravity, as measured by the inverse of the Bond number, up to a point when the entire interface is pinned ($h' = 0$). Here we show experimental measurements (symbols) and a best-fit straight line (solid black line).

the viscosity ratio ranges from $\mathcal{M} \approx 250$ to 2500. The liquids are all wetting to glass, and the choice of liquid exhibits only a small difference on the receding and advancing contact angles: $\theta_r \in [0^\circ, 16^\circ]$, $\theta_a \in [0^\circ, 23^\circ]$ (Fig. 4). Our experiments and analysis below show that, in this range, the contact angles are not leading-order parameters in the problem.

We understand the immiscible lock-exchange problem as a finite perturbation with respect to the miscible problem at the same value of \mathcal{M} . Assuming that the pinning length increases linearly with the strength of capillary forces relative to gravity, we suggest that $(h_s - h')/H \sim \text{Bo}^{-1}$, where h_s/H is exclusively a function of \mathcal{M} . This scaling relation is confirmed experimentally (Fig. 5). The value of h_s/H depends only weakly on the viscosity ratio \mathcal{M} [12], taking values between 0.585 and 0.587 for the viscosity ratios corresponding to our experiments (Fig. 5, inset). The lower hinge approaches the tilting point of the miscible problem when capillarity is negligible relative to gravity ($h' \rightarrow h_s$ as $\text{Bo}^{-1} \rightarrow 0$) and is equal to zero when the balance between capillary and gravity forces exceeds a certain threshold ($h' = 0$ for $\text{Bo}^{-1} \gtrsim 0.14$). In this latter scenario, the entire interface is pinned by capillarity and does not tilt, regardless of the precise value of contact angle.

B. Physics of capillary pinning

The scaling of the hinge height, however, says little about the underlying reason why the hinge and the pinned interface exist. We next show that the mechanistic cause of the pinning behavior is *capillary pressure hysteresis*. In our immiscible gravity-exchange flows, air spreads along the top boundary of the cell (a drainage front) while the viscous liquid spreads along the bottom (an imbibition front). For the air to invade each pore throat, its pressure P_{nw} (assumed atmospheric, P_{atm})

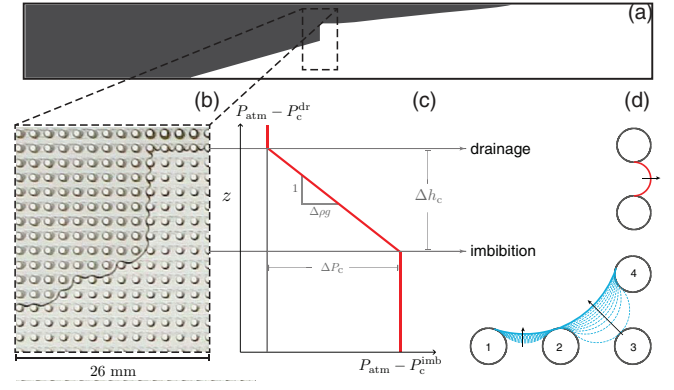


FIG. 6. (Color online) (a) Presence of a pinned interface in lock-exchange flow. Due to hysteresis effects, the capillary pressure at the drainage front (P_c^{dr}) is larger than the capillary pressure at the imbibition front (P_c^{imb}). Along the pinned vertical interface, the capillary pressure transitions from P_c^{imb} at the bottom to P_c^{dr} at the top. (b) Snapshot of the pinned interface of an immiscible lock exchange experiment (air/silicone oil) in a thin acrylic cell with a regular pattern of cylindrical posts simulating the pore-scale microstructure of a porous medium. The increase in capillary pressure (drop in wetting fluid pressure) from left to right is visible via the decrease in the radius of curvature along the interface. This increase in capillary pressure along the pinned interface is offset by the drop in hydrostatic pressure. (c) The solid red line shows a simple interpretation of the wetting phase pressure *along the interface*, as a function of elevation z . We assume the pressure in the air is atmospheric at all times. The wetting-phase interface pressure P_w^1 can be calculated by subtracting the capillary pressure from the air pressure ($P_w^1 = P_{\text{atm}} - P_c$). It is constant along the active drainage and imbibition fronts, and varies hydrostatically along the pinned interface. (d) Steady state interface configuration on the drainage side (solid red) and imbibition side (solid blue) of the pinned interface, along with the interface progression on the imbibition side (dashed blue), for a perfectly wetting imbibing fluid. Capillary pressure hysteresis is completely controlled by the pore geometry, due to the fundamental differences in the pore-level invasion events between drainage and imbibition, as a result, it is apparent even in the absence of contact angle hysteresis.

must, locally, exceed the pressure P_w in the liquid by an amount larger than or equal to the *drainage* capillary entry pressure P_c^{dr} [16]. Similarly, along the imbibition front, the liquid invades if $P_{nw} - P_w$ is less than the *imbibition* capillary pressure P_c^{imb} , which is always less than the drainage capillary pressure [2,16]. The pressure difference $\Delta P_c = P_c^{\text{dr}} - P_c^{\text{imb}}$ is recovered along a pinned portion of the interface between the drainage and imbibition fronts, which must therefore have height $\Delta h_c = \Delta P_c / (\Delta \rho g)$ (Fig. 6).

Although hysteresis in capillary pressure is sometimes caused by hysteresis in contact angle, such as for a raindrop pinned on a window, this is not the case here. In fluid flows through porous media, capillary pressure hysteresis is caused by the fundamental difference in the details of fluid invasion between drainage and imbibition: Invasion of nonwetting fluid produces strongly curved interfaces, whereas invasion of wetting fluid produces much flatter interfaces [16–20]. As a result, capillary pressure hysteresis is present even in the absence of contact angle hysteresis.

1. Micromodel experiments

The presence of capillary pressure hysteresis in the absence of contact angle hysteresis is well illustrated by the gravity-exchange flow of air and silicone oil in a thin acrylic cell, etched to form a regular pattern of cylindrical posts (Fig. 6). This system serves as a porous medium analog in the sense of introducing microstructure, but takes away the complexity of a random medium and permits visualizing the flow at the pore level.

At the top of the pinned portion of the interface, the air-silicone oil interface is just at the threshold of air invading and displacing the silicone oil. For slow flows, in which pore-scale dynamic effects due to the intermittent pressurization of the viscous fluid are small [21,22], the pressure difference between the fluids is equal to the *drainage* capillary entry pressure, P_c^{dr} , which, for zero contact angle ($\theta_r = 0^\circ$), is equal to $2\gamma/d$, where d is the distance between two neighboring posts (and, in our micromodel system, also equal to the diameter of the posts).

At the bottom of the pinned portion of the interface, the air-silicone oil interface adopts a “diagonal” configuration [between posts 2 and 4 in Fig. 3(d)], which is stable as long as the pressure difference between air and silicone oil is larger than some threshold value P_c^{imb} (an *imbibition* capillary entry pressure), which for our micromodel geometry and for zero contact angle is equal to $0.37\gamma/d$. Below this threshold capillary pressure, the interface is no longer pinned and would undergo *imbibition*.

2. Dependence of the amount of pinning on contact angle

The height of the pinned vertical interface, $\Delta h_c = (P_c^{\text{dr}} - P_c^{\text{imb}})/(\Delta\rho g)$, exhibits only a small dependence on contact angle. In the micromodel system, the height of the pinned interface takes the form

$$\Delta\rho g \Delta h_c = \gamma \left(\frac{1}{r_{\text{dr}}} - \frac{1}{r_{\text{imb}}} \right), \quad (1)$$

where γ is the interfacial tension, and r_{dr} and r_{imb} are the minimum and maximum radii of curvature achievable in drainage and in imbibition, respectively, which are functions of the receding and advancing contact angles, respectively, and of the pore geometry. We scale Δh_c by the cell height H , and r_{dr} and r_{imb} by the post diameter d :

$$\frac{\Delta h_c}{H} = \frac{\gamma/d}{\Delta\rho g H} \left(\frac{d}{r_{\text{dr}}} - \frac{d}{r_{\text{imb}}} \right). \quad (2)$$

The coefficient outside the parentheses on the right-hand side of Eq. (2) is the inverse of the Bond number. The term in parentheses measures the amount of hysteresis in the system, and is a function of both contact angle and pore geometry. Here we generalize the expressions of the radii of curvature that correspond to the drainage and imbibition entry capillary pressures in the micromodel for nonzero advancing and receding contact angles.

Consider four posts of diameter d , each a distance d apart from its nearest neighbors (Fig. 7). The interface must intercept the posts at an angle equal to the contact angle θ . Basic geometric considerations lead to expressions of the radius of curvature of the interfaces (r_1 and r_2) as a

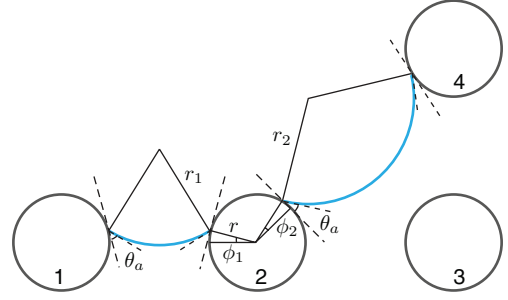


FIG. 7. (Color online) Interface configuration (solid blue) on the imbibition side of the exchange flow. We solve for the progression of the interface arcs as they advance through the pore by enforcing pressure continuity between posts 1,2 and 3,4 (i.e., $r_1 = r_2$). The interfaces merge and advance to the next set of posts when the two interface arcs touch (i.e., $\phi_1 + \phi_2 = 3/4\pi$). The diameter of the posts is d , and each post is one diameter away from its closest neighbors, the same as the design of the micromodel [Fig. 6(b)].

function of the contact angle θ and the subtended angles (ϕ_1 and ϕ_2):

$$r_1 = \frac{[2 - \cos(\phi_1)] d}{\cos(\phi_1 + \theta) \frac{d}{2}}, \quad (3)$$

$$r_2 = \frac{[2\sqrt{2} - \cos(\phi_2)] d}{\cos(\phi_2 + \theta) \frac{d}{2}}. \quad (4)$$

In drainage, $\theta = \theta_r$ and the drainage capillary entry pressure corresponds to the minimum radius of curvature r_1 : $r_{\text{dr}} = \min_{\phi_1} r_1(\phi_1; \theta_r)$.

In imbibition, $\theta = \theta_a$, and a sequence of stable configurations can be obtained by equating $r_1 = r_2$. This leads to a one-parameter family of solutions shown in Fig. 6(d). The imbibition capillary pressure corresponds to the configuration for which the two interfaces touch, that is, $r_{\text{imb}} = \{r_1(\phi_1; \theta_a) \text{ such that } r_1(\phi_1; \theta_a) = r_2(\phi_2; \theta_a) \text{ and } \phi_1 + \phi_2 = 3\pi/4\}$.

In Fig. 8 we show the dependence of the dimensionless quantity $d/r_{\text{dr}} - d/r_{\text{imb}}$ as a function of advancing contact

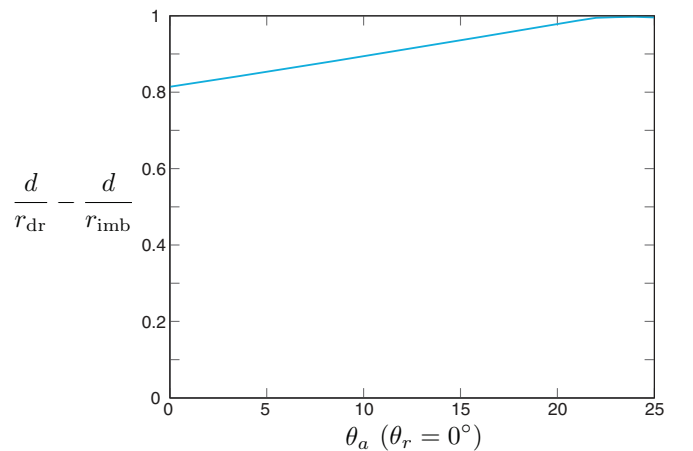


FIG. 8. (Color online) Dependence of the dimensionless quantity $d/r_{\text{dr}} - d/r_{\text{imb}}$ controlling the magnitude of the pinned interface in our micromodel system, as a function of advancing contact angle θ_a , assuming $\theta_r = 0^\circ$.

angle θ_a , assuming $\theta_r = 0^\circ$. This quantity exhibits only a small dependence on the contact angles.

IV. INTERFACE PINNING: DYNAMICS

A. Macroscopic sharp-interface model

To capture the dynamic macroscopic behavior of immiscible gravity-exchange flows, we propose a simple theoretical model based on the classical sharp-interface model [11,12]. The mathematical model is a partial differential equation for the height of the interface, which assumes a hydrostatic pressure distribution everywhere (known as vertical flow equilibrium, or VFE [23]) and Darcy flow to link flow velocity and pressure gradients. In a related context, the classical model has been modified to replace the sharp interface by a capillary transition zone [24–26]. Here we extend the model to include capillary pressure *hysteresis* while, in agreement with our experiments, retaining the sharp-interface approximation.

We consider exchange flow between a buoyant nonwetting fluid with density $\rho_1 = \rho$ and a dense wetting fluid with density $\rho_2 = \rho + \Delta\rho$ in a horizontal porous layer of thickness H (Fig. 9). We assume that the porous medium is homogeneous and isotropic with permeability k and porosity ϕ , and that the boundaries of the flow domain are impermeable. Since we assume that the two fluids are separated by a sharp interface, the thickness of the fluid layers must sum to the thickness of the porous layer everywhere, $h_1 + h_2 = H$. By assuming hydrostatic pressure in both fluids, we can express the pressure distribution in the layer as

$$P = \begin{cases} P_I - \rho g(z - h_2) & \text{for } z > h_2 \\ P_I - P_c + (\rho + \Delta\rho)g(h_2 - z) & \text{for } z \leq h_2 \end{cases}, \quad (5)$$

where P_I is the unknown pressure at the interface and g is the gravitational acceleration. By definition, the pressure difference across the interface between the nonwetting fluid and the wetting fluid is the capillary pressure P_c .

The volumetric flux per unit width of fluid phase i is given by Darcy's law $q_i = -k\lambda_i \partial P / \partial x$, where $\lambda_i = k_{r,i} / \mu_i$ is the mobility of the fluid phase and $k_{r,i}$ is the relative permeability to that phase. Since we assume the two fluid phases to be completely segregated, the relative permeabilities are equal to

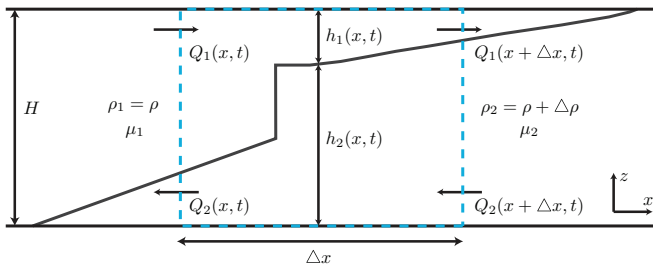


FIG. 9. (Color online) We develop a sharp interface model for the exchange flow between a buoyant, nonwetting fluid and a dense, wetting fluid, separated initially by a vertical interface. We assume Darcy flow within each fluid and hydrostatic pressure distribution everywhere. We then solve for the model by enforcing conservation of volume in a control volume (dashed blue). The resulting model is a partial differential equation for the height of the interface as a function of time.

one. The flow rate is given by the product of the thickness of the fluid phase and its volumetric flux, $Q_i = h_i q_i$. Hence, we obtain

$$Q_1 = -h_1 k \lambda_1 \left(\frac{\partial P_I}{\partial x} - \rho g \frac{\partial h_1}{\partial x} \right), \quad (6a)$$

$$Q_2 = -h_2 k \lambda_2 \left[\frac{\partial P_I}{\partial x} - (\rho + \Delta\rho)g \frac{\partial h_2}{\partial x} - \frac{\partial P_c}{\partial x} \right]. \quad (6b)$$

Imposing global volume conservation ($Q_1 + Q_2 = 0$), we solve for $\partial P_I / \partial x$ and substitute into Eq. (6) to obtain the flow rates of both fluids. Since $h_1 + h_2 = H$, we can express the flow rates in terms of only h_2 , which also represents the height of the interface:

$$Q_2 = \frac{\Delta\rho g k}{\mu_2} (1 - f) h_2 \left(\frac{\partial h_2}{\partial x} - \frac{\partial P_c / \Delta\rho g}{\partial x} \right), \quad (7a)$$

$$f = \frac{h_2}{h_2 + \mathcal{M}(H - h_2)}, \quad (7b)$$

where f is the fractional flow function and $\mathcal{M} = \mu_2 / \mu_1$ is the viscosity ratio. To obtain an equation for the evolution of the interface, we consider the conservation of volume of the dense fluid over region Δx and time Δt (Fig. 9). The change in volume of the dense fluid is given by

$$\Delta V_2 = \Delta h_2 \Delta x \phi = (Q_2|_{x+\Delta x} - Q_2|_x) \Delta t. \quad (8)$$

Inserting Eq. (7) into Eq. (8) and taking limits for small Δx and Δt , we get the partial differential equation for the evolution of the interface height $h \equiv h_2$:

$$\frac{\partial h}{\partial t} - \kappa \frac{\partial}{\partial x} \left[(1 - f) h \left(\frac{\partial h}{\partial x} - \frac{\partial h_c}{\partial x} \right) \right] = 0, \quad (9)$$

where $\kappa = \Delta\rho g k / (\mu_2 \phi)$ is the characteristic buoyancy velocity and $h_c = P_c / \Delta\rho g$ is the capillary height.

The function $g(h; \mathcal{M}) \equiv (1 - f(h; \mathcal{M}))h$ in Eq. (9) can be interpreted as a nonlinear diffusion coefficient. It is well behaved for all finite (even large) values of \mathcal{M} (Fig. 10). In the

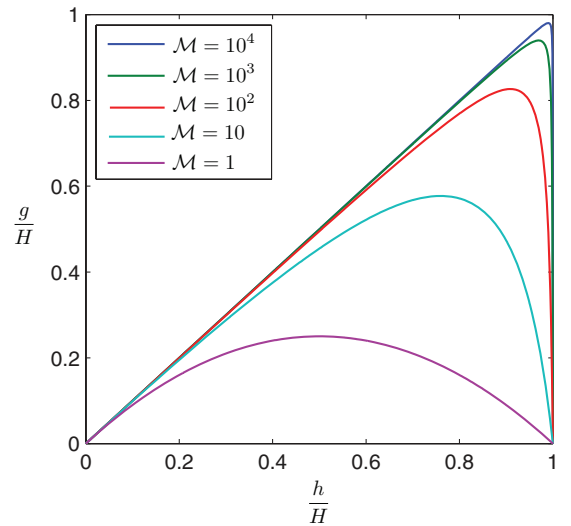


FIG. 10. (Color online) The dimensionless nonlinear diffusion coefficient $g(h; \mathcal{M})/H \equiv (1 - f(h; \mathcal{M}))h/H$ in Eq. (9) as a function of the dimensionless height of the interface h/H for several values of viscosity ratio \mathcal{M} .

limit $\mathcal{M} \rightarrow \infty$, application of the L'Hôpital rule indicates that $g_\infty(h) \equiv \lim_{\mathcal{M} \rightarrow \infty} g(h; \mathcal{M}) = h$, which is the well-known limit for a viscous fluid slumping against a horizontal surface in an inviscid ambient fluid [13,27]. Our experiments, however, always correspond to a finite value of \mathcal{M} .

We take P_c to be some characteristic drainage capillary pressure P_c^{dr} , where the nonwetting fluid displaces the wetting fluid, and some characteristic imbibition capillary pressure P_c^{imb} , where the wetting fluid displaces the nonwetting fluid. Across the pinned interface, P_c jumps from P_c^{dr} to P_c^{imb} . Since we have constant capillary pressures along the active drainage and imbibition fronts, $\partial h_c / \partial x = 0$. Therefore, $\partial h_c / \partial x \neq 0$ only along the pinned interface. In other words, it introduces a jump $[[h_c]]$ in the interface height of magnitude $(P_c^{\text{dr}} - P_c^{\text{imb}}) / (\Delta \rho g)$.

We solve Eq. (9) for the interface height h , subject to an initial condition that approximates a step function from $h = 0$ for $x < 0$ to $h = 1$ for $x > 0$, and no-flow boundary conditions ($\partial h / \partial x = 0$) at the ends of the cell. We solve the equation numerically using a centered finite volume method in space with forward Euler time integration.

The capillary pressure term vanishes everywhere except at the nodes that separate the portion of the interface that is in drainage from the portion that is in imbibition. Here the capillary pressure term contributes a finite jump in the flux across these two nodes, and this jump causes a sharp step in the height of the interface.

B. Simulation of lock-exchange flows

The shape of the interface predicted by our model exhibits good agreement with the experiment (Fig. 1). We measure *a priori* all the parameters in the model (porosity, permeability, fluid densities, and viscosities) except for $[[h_c]]$, which we obtain by measuring the length of the pinned interface in the experiment.

Additionally, the model predicts quantitatively the time evolution of the nose position of both currents: the buoyant nonwetting current [Fig. 11(a)] and the dense wetting current [Fig. 11(b)]. It is encouraging that our mathematical description, which assumes horizontal flow, predicts accurately a lock exchange where clearly there is vertical flow since a portion of the interface remains pinned (and therefore vertical) at all times. Capillarity reduces the gravity-exchange flow rate (and as a result slows down the process), but the nonwetting and wetting currents still advance in a way that is well described by the $x \sim t^{1/2}$ scaling of the miscible lock exchange before they hit the cell boundaries (Fig. 11).

C. Simulation of finite-release gravity currents

The impact of interface pinning effects due to capillary hysteresis is most pronounced when the initial interface is close to one of the lateral boundaries. In this case, one of the currents hits the boundary early and the process models a finite-volume release. The finite release of a miscible buoyant fluid spreads indefinitely [12]. In contrast, a finite volume of immiscible fluid spreads up to a finite distance at which the hydrostatic pressure difference that drives the flow is exactly balanced by the difference in capillary pressures at the drainage

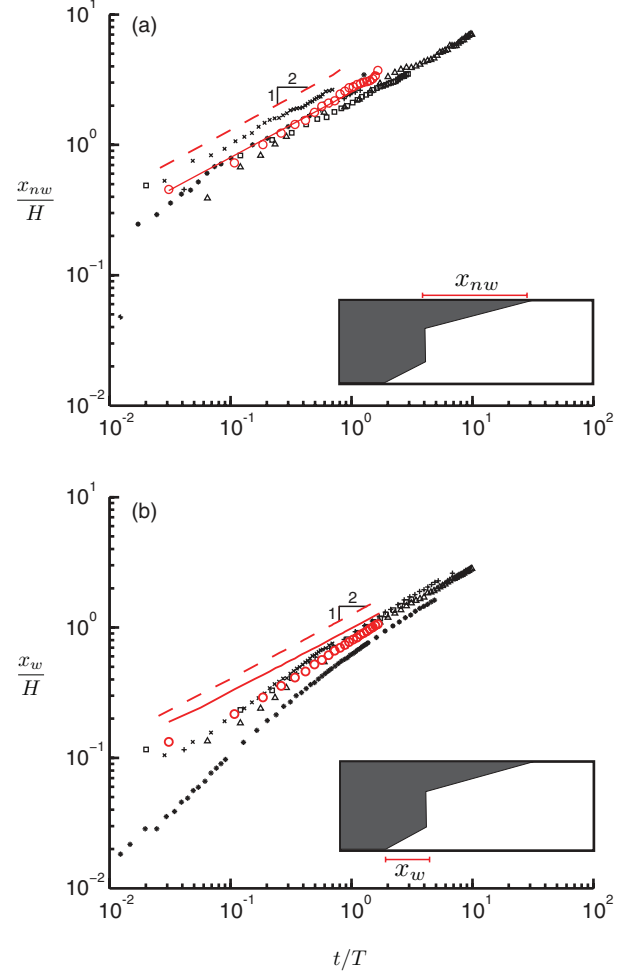


FIG. 11. (Color online) Time evolution of the nose positions of the (a) buoyant nonwetting current, and (b) dense wetting current, measured relative to the position of the initial vertical interface. We scale nose position by the cell height H and time by the characteristic time $T = H/\kappa$. We show the data for five experiments with different values of Bo^{-1} (black symbols: $\times = 0.021$; $*$ = 0.028; $\square = 0.029$; $\triangle = 0.041$). For a particular experiment ($\text{Bo}^{-1} = 0.052$; $\mathcal{M} = 2580$), we compare the nose positions from the experiment (red circles) with those computed with our model (red solid line). We also show nose positions from the numerical solution to the miscible flow model ($[[h_c]] \rightarrow 0$; dashed line).

and imbibition fronts. In other words, capillary hysteresis stops the gravity current (Fig. 12).

V. DISCUSSION: RELEVANCE TO CO₂ SEQUESTRATION

The potential for capillary pinning to stop a spreading gravity current is particularly relevant in the context of CO₂ sequestration, where CO₂ is injected into aquifers saturated with denser and more viscous groundwater. During and after injection, the difference in density between the two fluids will drive a gravity-exchange flow [5–7], increasing the lateral extent of the CO₂ plume and the risk that the CO₂ will encounter a fault or fracture through which it could leak. Deep saline aquifers are naturally water-wet and, therefore, the hysteresis behavior will be similar [28–30]. The vertical-flow

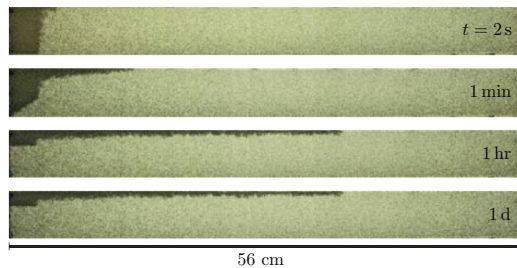


FIG. 12. (Color online) Finite release of a buoyant, nonwetting fluid (air) in a porous medium filled with a dense, wetting fluid (silicone oil). The dense, wetting front hits the left boundary, changing the spreading behavior of the buoyant current. Capillary hysteresis is responsible for the pinning of the initial interface and, ultimately, for stopping the buoyant plume at a finite distance, in stark contrast with a miscible plume which would continue to spread indefinitely.

equilibrium assumption is also appropriate in the field setting due to the very large aspect ratio L/H of aquifers. Therefore, transfer of the results depends on the values of $\text{Bo}^{-1} = \gamma/(\Delta\rho g H d)$ in the field. The value of the interfacial tension γ is relatively insensitive to depth and is ~ 0.025 N/m [31], and the density difference $\Delta\rho$ varies between 250 and 500 kg/m³ for deep and shallow aquifers, respectively [32]. Large capillary effects occur in aquifers that are deep

($\Delta\rho \sim 250$ kg/m³), either thin or vertically disconnected by low-permeability shale layers ($H \sim 10$ m), and have small grain sizes ($d \sim 10$ μm). In contrast, small capillary effects correspond to aquifers that are shallow ($\Delta\rho \sim 500$ kg/m³) and thick ($H \sim 100$ m) and have large grain sizes ($d \sim 50$ μm). Thus, $\text{Bo}^{-1} \in [0.001, 0.1]$, a range that exhibits a large overlap with our experimental conditions (Fig. 5). Even though the shape of the CO₂ plume after the injection period does matter quantitatively [33], the fundamental qualitative impact of the capillary pinning phenomenon is already present in the lock-exchange flow configuration. This suggests that capillary pinning is possibly an important, yet unexplored, trapping mechanism during geologic CO₂ sequestration.

ACKNOWLEDGMENTS

We thank Prof. Gareth McKinley for facilitating the contact-angle measurements (Fig. 4). This work was partly funded by the US Department of Energy (Grants DE-SC0003907 and DE-FE0002041) and the MIT/Masdar Institute Program. Additional funding was provided by the MIT Energy Fellows Program (to B.Z.), the Martin Family Society of Fellows for Sustainability and a David Crighton Fellowship (to C.W.M.), a Royal Society University Research Fellowship (to J.A.N.), the Royal Society Wolfson Research Merit Award (to H.E.H.), the Reed Research Fund, and the ARCO Chair in Energy Studies (to R.J.).

- [1] R. M. Iverson, *Rev. Geophys.* **35**, 245 (1997).
- [2] J. Bear, *Dynamics of Fluids in Porous Media* (Elsevier, New York, 1972).
- [3] A. Oron, S. H. Davis, and S. G. Bankoff, *Rev. Mod. Phys.* **69**, 931 (1997).
- [4] J. M. Nordbotten, M. A. Celia, and S. Bachu, *J. Fluid Mech.* **561**, 307 (2006).
- [5] M. Bickle, A. Chadwick, H. E. Huppert, M. Hallworth, and S. Lyle, *Earth Planet. Sci. Lett.* **255**, 164 (2007).
- [6] M. A. Hesse, F. M. Orr, Jr., and H. A. Tchelepi, *J. Fluid Mech.* **611**, 35 (2008).
- [7] R. Juanes, C. W. MacMinn, and M. L. Szulczewski, *Transp. Porous Media* **82**, 19 (2010).
- [8] S. E. Gasda, J. M. Nordbotten, and M. A. Celia, *Water Resour. Res.* **47**, W05528 (2011).
- [9] C. W. MacMinn, M. L. Szulczewski, and R. Juanes, *J. Fluid Mech.* **688**, 321 (2011).
- [10] M. L. Szulczewski, C. W. MacMinn, H. J. Herzog, and R. Juanes, *Proc. Natl. Acad. Sci. USA* **109**, 5185 (2012).
- [11] H. E. Huppert and A. W. Woods, *J. Fluid Mech.* **292**, 55 (1995).
- [12] M. A. Hesse, H. A. Tchelepi, B. J. Cantwell, and F. M. Orr, Jr., *J. Fluid Mech.* **577**, 363 (2007).
- [13] G. I. Barenblatt, *Scaling, Self-Similarity, and Intermediate Asymptotics* (Cambridge University Press, Cambridge, 1996).
- [14] P. G. de Gennes, *Rev. Mod. Phys.* **57**, 827 (1985).
- [15] D. Bonn, J. Eggers, J. Indekeu, J. Meunier, and E. Rolley, *Rev. Mod. Phys.* **81**, 739 (2009).
- [16] R. Lenormand, C. Zarcone, and A. Sarr, *J. Fluid Mech.* **135**, 123 (1983).
- [17] M. Cieplak and M. O. Robbins, *Phys. Rev. B* **41**, 11508 (1990).
- [18] N. Martys, M. Cieplak, and M. O. Robbins, *Phys. Rev. Lett.* **66**, 1058 (1991).
- [19] N. C. Wardlaw and Y. Li, *Transp. Porous Media* **3**, 17 (1988).
- [20] C. D. Tsakiroglou and A. C. Payatakes, *Adv. Colloid Interface Sci.* **75**, 215 (1998).
- [21] K. J. Måløy, L. Furuberg, J. Feder, and T. Jøssang, *Phys. Rev. Lett.* **68**, 2161 (1992).
- [22] L. Xu, S. Davies, A. B. Schofield, and D. A. Weitz, *Phys. Rev. Lett.* **101**, 094502 (2008).
- [23] Y. C. Yortsos, *Transp. Porous Media* **18**, 107 (1995).
- [24] L. W. Lake, *Enhanced Oil Recovery* (Prentice-Hall, Englewood Cliffs, NJ, 1989).
- [25] J. M. Nordbotten and H. K. Dahle, *Water Resour. Res.* **47**, W02537 (2011).
- [26] M. J. Golding, J. A. Neufeld, M. A. Hesse, and H. E. Huppert, *J. Fluid Mech.* **678**, 248 (2011).
- [27] G. I. Barenblatt, *App. Math. Mech.* **16**, 67 (1952) [*Prikl. Mat. Mekh.* **16**, 67 (1952)].
- [28] P. H. Valvatne and M. J. Blunt, *Water Resour. Res.* **40**, W07406 (2004).
- [29] R. Juanes, E. J. Spiteri, F. M. Orr, Jr., and M. J. Blunt, *Water Resour. Res.* **42**, W12418 (2006).
- [30] C. H. Pentland, R. El-Maghraby, S. Iglauer, and M. J. Blunt, *Geophys. Res. Lett.* **38**, L06401 (2011).
- [31] C. Chalbaud, M. Robin, J.-M. Lombard, F. Martin, P. Egermann, and H. Bertin, *Adv. Water Resour.* **32**, 98 (2009).
- [32] S. Bachu, *Environ. Geol.* **44**, 277 (2003).
- [33] C. W. MacMinn and R. Juanes, *Comput. Geosci.* **13**, 483 (2009).